Int J Adv Manuf Technol (2016) 84:2479–2489
DOI 10.1007/s00170-015-7913-5

ORIGINAL ARTICLE

Modeling of tool influence function for high-efficiency polishing

X. L. Ke[1,2] · C. J. Wang[1,3] · Y. B. Guo[1] · Q. Xu[3]

Received: 18 May 2015 / Accepted: 24 September 2015 / Published online: 3 October 2015
© Springer-Verlag London 2015

Abstract The M-shaped tool influence function (TIF) usually comes out when adopting a large tool offset at the high-efficiency polishing stage in bonnet polishing. Its modeling is as important as the Gaussian-like TIF for the polishing process. However, the existing reports on the TIF of bonnet polishing are mostly about the Gaussian-like TIF model, or the model which cannot accurately simulate the M-shaped TIF. Viewing this, an optimized TIF model about the semirigid (SR) bonnet tool is presented based on the finite element analysis method which can be used to model both M-shaped and Gaussian-like TIFs. The verification experiments show that the simulated TIFs based on this model are in good agreement with the actual measured TIF. The relative deviation between them is about only 5 % in terms of root mean square value of the residual error.

Keywords Tool influence function · Bonnet polishing · High-efficiency polishing · Simulation · FEA

✉ C. J. Wang
wcj-2000@163.com

X. L. Ke
kexiaolong@xmu.edu.cn

Y. B. Guo
guoyb@xmu.edu.cn

Q. Xu
xuqiao@vip.sina.com

[1] Department of Mechanical and Electrical Engineering, Xiamen University, Xiamen 361005, China

[2] School of Mechanical and Automotive Engineering, Xiamen University of Technology, Xiamen 361024, China

[3] Research Center of Laser Fusion, China Academy of Engineering Physics, Mianyang 621900, China

1 Introduction

By virtue of high polishing efficiency and conformability to the freeform surfaces, bonnet polishing (BP) technology has become more and more popular in polishing aspheric surfaces used for large telescopes [1–5], artificial joints [6], etc. As a member of the sub-aperture deterministic polishing technology, modeling of the tool influence function (TIF) plays an important role in the manufacturing process. With the TIF model, the process generation and measurement of a real TIF on a test part can be omitted, which shortens the production cycle. Besides, it is usually inconvenient to measure large-size TIF [7]. Hence, TIF of the deterministic sub-aperture polishing is usually modeled when studying this technology, such as pitch tool polishing [8], ion beam finishing [9], magnetorheological finishing [10, 11], fluid jet polishing [12, 13], rigid conformal lap polishing [14], etc.

For bonnet polishing, measured TIF was adopted at the early development stage of this process [3]. Then, Kim et al. [15] presented the theoretical model to simulate TIF, but the pressure distribution in this model needs to be estimated based on the measured TIF. Furthermore, Li et al. [16] built the TIF model based on the finite element analysis (FEA) method. However, the solid rubber spherical part was adopted in this simulation model, which cannot truly represent the membrane bonnet and cannot simulate the bonnet under a different inner pressure. To solve this problem, Wang et al. [17] rebuilt the simulation model whose structure is more close to that of the real bonnet tool. The final contact pressure was generated based on the contact pressure along the section line fitted adopting the Gaussian-like function. However, this model can only be effective when the TIF shape is Gaussian like. When high-efficiency polishing is needed at the early stage, large tool offset is usually adopted which makes the TIF become M shaped.

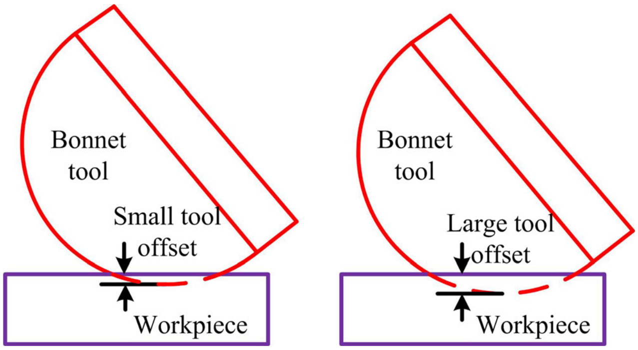

Fig. 1 Schematic explanation about small and large tool offset

Lately, we demonstrated a semirigid (SR) bonnet tool which can implement much higher material removal rate than the flexible bonnet [18]. Here, we introduce a TIF model of the optimized SR bonnet tool, which can accurately simulate both Gaussian-like and M-shaped TIFs. Section 2 introduces the theoretical background including the material removal principle and comparison of the surface form error uniform removed by the Gaussian-like TIF and M-shaped TIF. Section 3 demonstrates the simulation model of the contact pressure. Section 4 simulates the TIF model, and experimental verifications are conducted in Section 5, leading to the conclusions in Section 6.

2 Theoretical background

In bonnet polishing, the amount of the removed material $H(x, y)$ is equal to the two-dimensional convolution between the TIF per unit time $R(x, y)$ and the dwell time function $D(x, y)$, along with the motion track [5]:

$$H(x,y) = R(x,y)**D(x,y) \tag{1}$$

If $H_0(x, y)$ is the amount of material needed to be removed, then the surface residual error $E(x, y)$ would be expressed as

$$E(x,y) = H_0(x,y) - R(x,y)**D(x,y) \tag{2}$$

It is well known that Gaussian-like TIF is conducive to the convergence of the surface form error in corrective polishing. As for bonnet polishing, its TIF shape depends on the tool offset used in the polishing process. (Tool offset is the distance of the tool compressed to the workpiece). Figure 1 schematically demonstrates the situations with small tool offset and large tool offset. Small tool offset is usually adopted in corrective polishing to generate Gaussian-like TIF. But in the pre-polishing stage, polishing efficiency is prior to the surface accuracy. M-shaped TIFs induced by large tool offset are usually adopted in this stage to implement a higher material removal rate. Gaussian-like TIF and M-shaped TIF generated by the bonnet tool have been presented in Fig. 2. Both of them

Fig. 2 TIF profiles. **a** Gaussian-like TIF, **b** M-shaped TIF

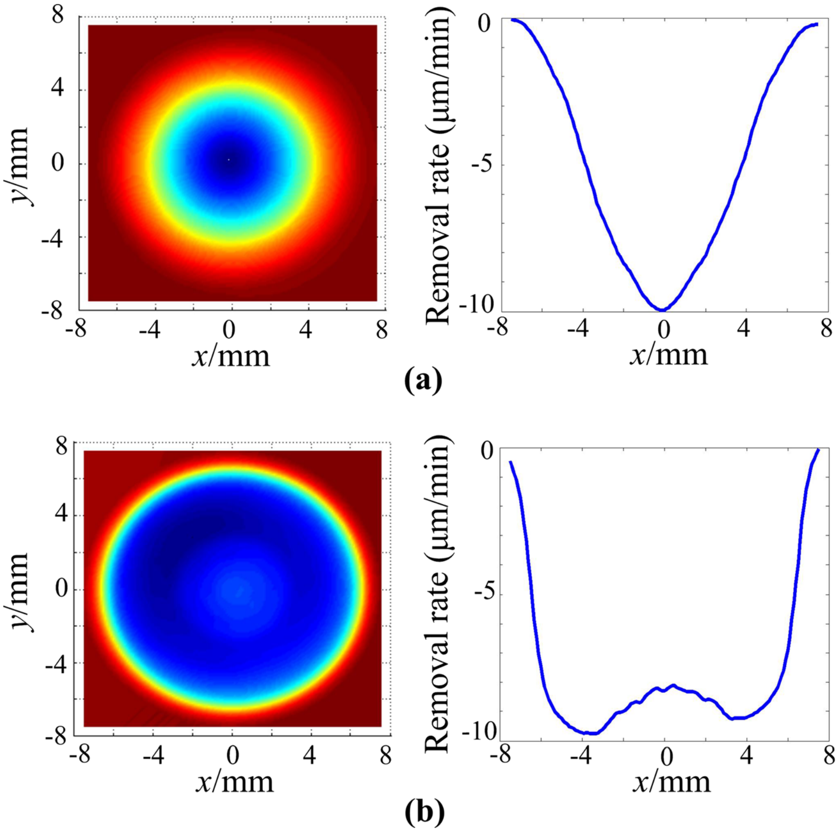

have been processed to have the same peak material removal rate which is −10 μm/min, and the diameter of them is 15 mm. The left part of Fig. 2 is the top view of the three-dimensional TIF and the right part is the sectional profile of them.

The uniform removal processes adopting these two TIFs were simulated according to Eq. (2). The size of the removal area is 50×50 mm^2 and distances between each dwell point in x and y directions are both 2 mm. Dwell time at each point is 0.2 s. Figure 3 demonstrates the surface residual error of their central 10×10 mm^2 zone. Figure 3a shows the surface residual error generated adopting the Gaussian-like TIF. The peak-to-valley (PV) value is 3 nm and the root mean square (RMS) value is 0.5 nm. The surface residual error generated adopting M-shaped TIF is larger than that generated adopting Gaussian-like TIF as shown in Fig. 3b, whose PV is 22.2 nm. But the form error at this accuracy is high enough to meet the requirement of pre-polishing.

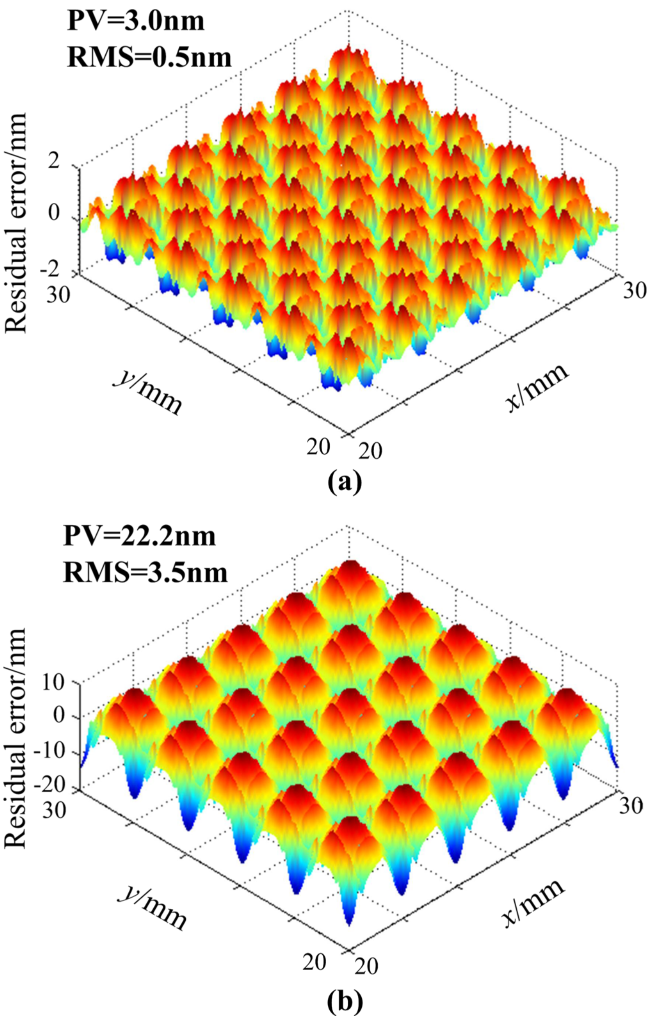

Fig. 3 Simulated surface residual error after uniform removal adopting different TIFs. **a** Adopt Gaussian-like TIF, **b** adopt M-shaped TIF

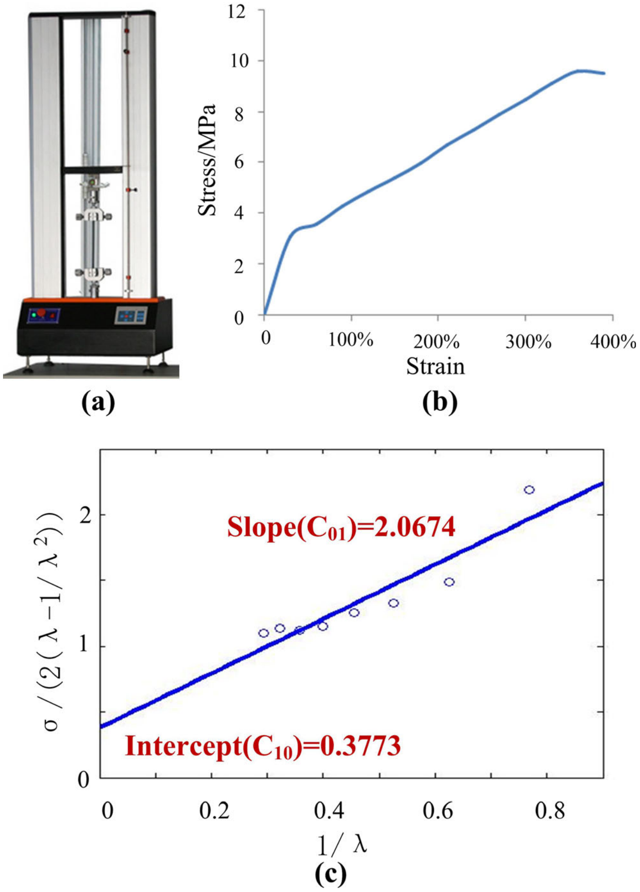

Fig. 4 **a** Uniaxial tension test equipment, **b** tested stress–strain curve of the rubber material, c Mooney–Rivlin plot based on the stress strain test data

Hence, the M-shaped TIF can be used to achieve high polishing efficiency in the pre-polishing process, leading to the TIF model being as important as the Gaussian-like TIF.

BP is one of the loose abrasive polishing processes whose material removal mechanism also can be expressed by the well-known Preston equation

$$\mathrm{d}z/\mathrm{d}t = kpv \tag{3}$$

where dt is the dwell time, dz is the material removal amount during the dwell time, k is the removal coefficient, p is the

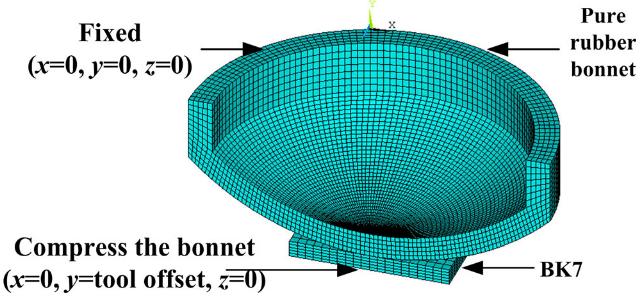

Fig. 5 Contact force simulation model of the pure rubber bonnet

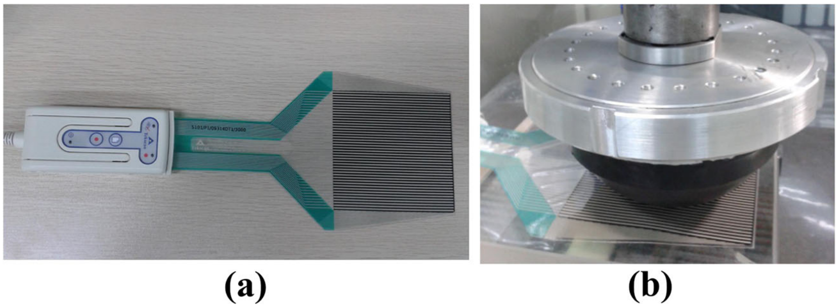

Fig. 6 **a** Texscan thin-film pressure sensor, **b** testing photograph

polishing pressure, and v is the relative velocity between the tool and the workpiece. Then, TIF in the unit time $TR(x, y)$ can be expressed as

$$R(x,y)=\frac{1}{T}\int_{0}^{T}k\cdot p(x,y)\cdot v(x,y)\cdot \mathrm{d}t \tag{4}$$

Hence, TIF can be determined through Eq. (4) if the polishing pressure distribution $p(x, y)$ and the relative velocity distribution $v(x, y)$ can be obtained.

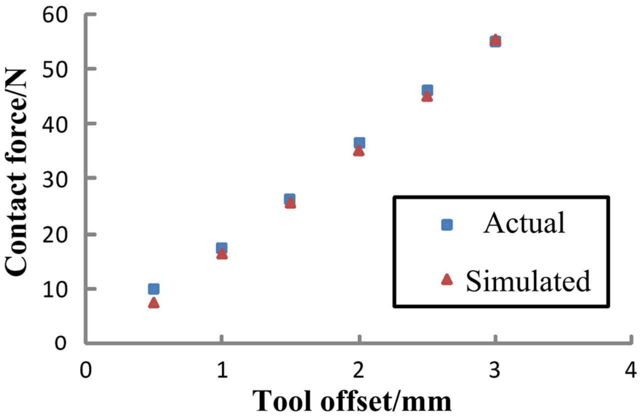

Fig. 7 Comparison between the tested contact force and simulated force

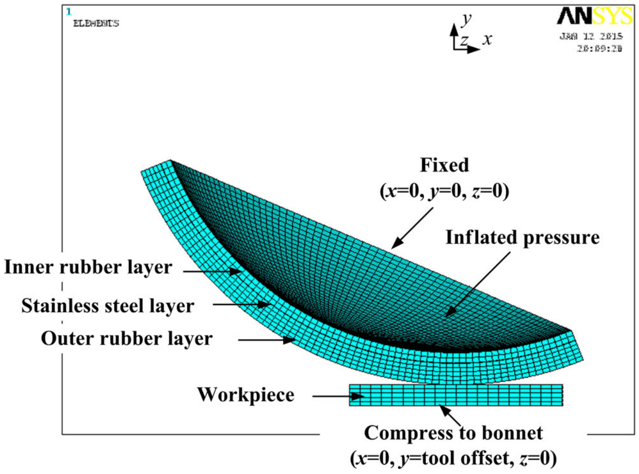

Fig. 8 Contact pressure simulation model of the SR bonnet

3 Simulation of the contact pressure

Measurement of the contact pressure is still not that easy and it is usually simulated through FEA [14–17]. Material characteristics used in the simulation can critically influence the simulation results. Hence, accurate characteristics of them should be determined firstly.

3.1 Determination of the rubber material coefficients

Rubber material is one of the hyperelastic materials, and its characteristic usually varies with its components. Uniaxial tension test [19] was conducted to obtain the stress–strain data of the rubber material. Figure 4a shows the testing equipment and the stress–strain test curve has been fitted in Fig. 4b. According to the Mooney–Rivlin method, two coefficients

Table 1 Material parameters

Materials	Parameters	Values
Rubber	C_{10}	0.3773
	C_{01}	2.0674
	Density (kg/m^3)	1.4×10^3
Stainless steel	Elastic modulus (MPa)	1.93×10^5
	Poisson ratio	0.29
	Density (kg/m^3)	8.0×10^3
	Tangent modulus (MPa)	7.7×10^4
BK7	Elastic modulus (MPa)	8.1×10^4
	Poisson ratio	0.206
	Density (kg/m^3)	2.51×10^3

Table 2 Simulation conditions

Conditions	Values
Bonnet radius (mm)	80
Precession angle (deg)	23
Tool offset (mm)	0.5, 1.6, 2.0
Inflated pressure (MPa)	0.25

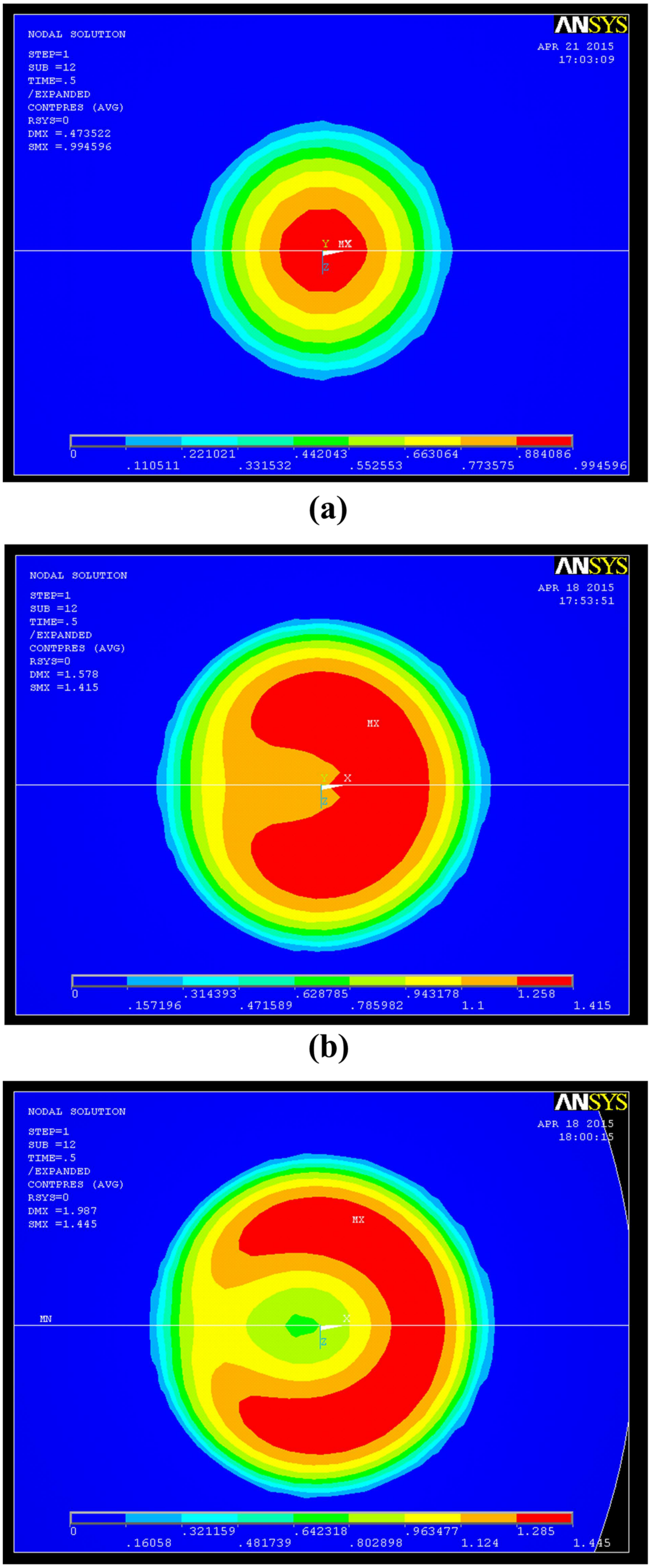

Fig. 9 Simulation results of the contact pressure under different tool offsets. **a** Tool offset=0.5 mm, **b** tool offset=1.6 mm, **c** tool offset=2.0 mm

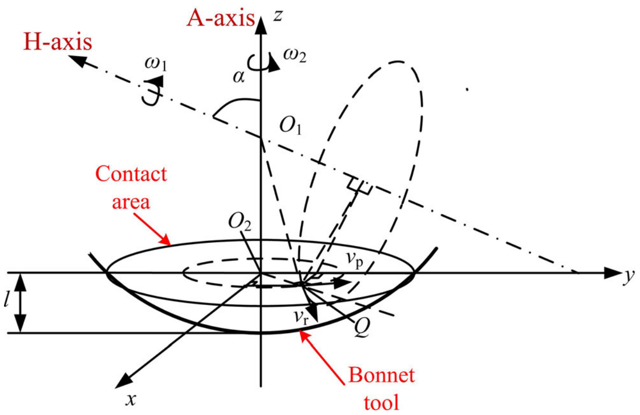

Fig. 10 Schematic diagram of the precession bonnet tool [17]

C_{10} and C_{01} of the rubber material can be determined through combining the following equation [20]:

$$\frac{\sigma}{2\left(\lambda-\lambda^{-2}\right)}=C_{10}+\frac{C_{01}}{\lambda} \tag{5}$$

where σ is the engineering stress and λ is the strain ratio. Equation (5) indicates that the plot of $\sigma/[2(\lambda-\lambda^{-2})]$ against λ^{-1} (so-called Mooney–Rivlin plot) gives a linear relation. Hence, C_{10} and C_{01} can be obtained from the intercept and slope, respectively. The Mooney–Rivlin plot has been presented in Fig. 4c and the obtained C_{10} is 0.3773 and C_{01} is 2.0674.

To verify the material coefficients of the rubber material, the simulation of the contact pressure using pure rubber was conducted and its calculated contact force was compared to the tested results of the real contact force. Figure 5 shows the simulation model. Noninflated pressure was loaded on the bonnet to exclude the influence of the deformation. A series of simulations with the tool offsets varying from 0.5 to 3 mm were conducted. Then, the contact forces under different tool offsets were tested using Texscan$^{\mathrm{TM}}$ thin-film pressure sensor as shown in Fig. 6a. The pure rubber bonnet tool without the polishing pad was used in this test corresponding to the simulation as shown in Fig. 6b. Comparison of the simulation and testing results of the contact force has been presented in Fig. 7.

According to the results in Fig. 7, the simulated contact forces under different tool offsets are almost the same with the actual contact force, which proves that the acquired material coefficients of the rubber material are correct.

3.2 Simulation model

Figure 8 shows the simulation model of the contact pressure for the SR bonnet. Half of the model was analyzed to simplify the calculation process, and the polishing pad was not considered as usual [17]. All DOFs of the fringe areas of all layers were set to zero to fix the bonnet. The distance of the workpiece compressed to the bonnet was defined through controlling the tool offset value. The inflated pressure is loaded on the inner rubber layer. Table 1 shows the material parameters utilized in this simulation, and simulation conditions are listed in Table 2.

3.3 Simulation results of the contact pressure

Figure 9 shows the contact pressure results of situations under three different tool offsets. It is noted that the contact pressure is rotational symmetric and Gaussian like when the tool offset is small. And its shape becomes asymmetric under a larger tool offset due to the larger impact of the fixed fringe. Zeng and Blunt [21] pointed out that the aluminum framework of the bonnet tool can influence the width of TIF. From this result, we can see that it also influences the pressure distribution. Besides, the pressure distribution shape turns into the tilted M shape when adopting larger tool offsets.

Fig. 11 Three different movement styles of bonnet polishing

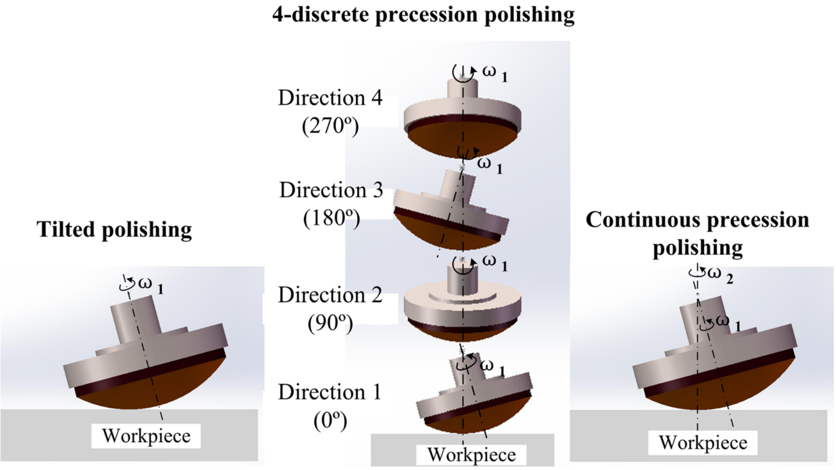

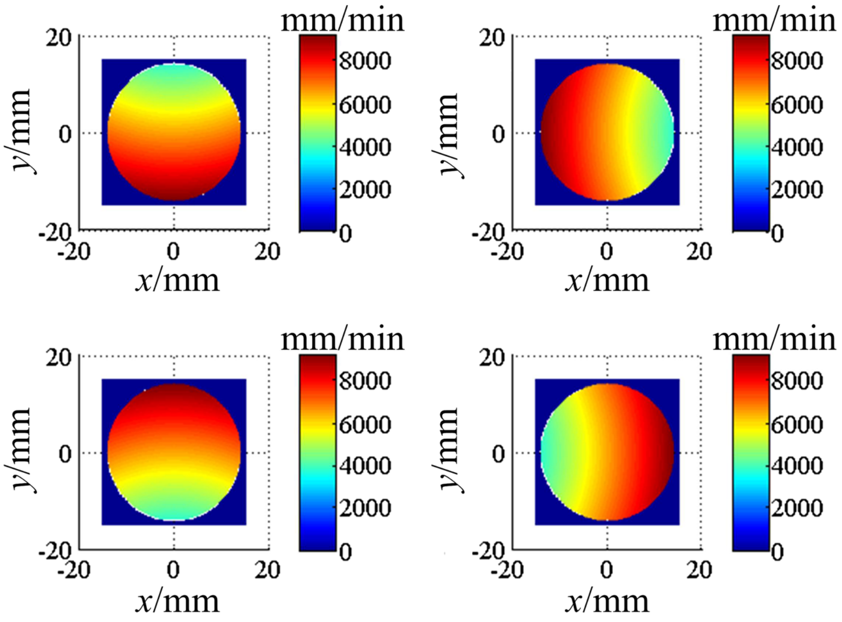

Fig. 12 Velocity distribution in four directions (tool offset= 1.6 mm)

4 Modeling of TIF

4.1 Velocity distribution model

In order to determine polishing velocity in the contact area, the schematic diagram of the precession bonnet tool is built in Fig. 10. Q is a point in the contact area, v_r is the velocity of point Q derived from the rotation of the H-axis, v_p is the velocity of point Q derived from the rotation of the A-axis, ω_1 is the rotation speed of the H-axis, ω_2 is the rotation speed of the A-axis, O_1 is the center of the bonnet tool, O_2 is the center of the contact area, l is the tool offset of the bonnet, and α is the precession angle [17].

Figure 11 demonstrates three different movement styles of bonnet polishing. Continuous precession polishing can generate Gaussian-like TIF and disordered surface texture to restrain mid-spatial frequency error, but it cannot be commonly used due to its high requirements for the polishing machine [22, 23]. Hence, in the real polishing process, it is usually replaced by discrete precession polishing which integrates several times of tilted polishing as shown in Fig. 11. The middle part of Fig. 11 shows the 4-discrete precession

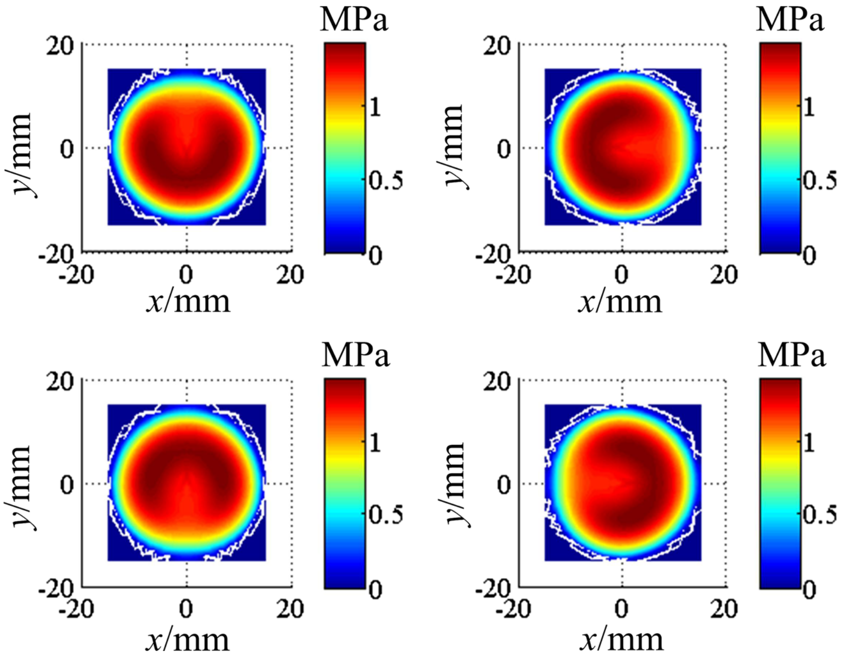

Fig. 13 Contact pressure distribution in four directions

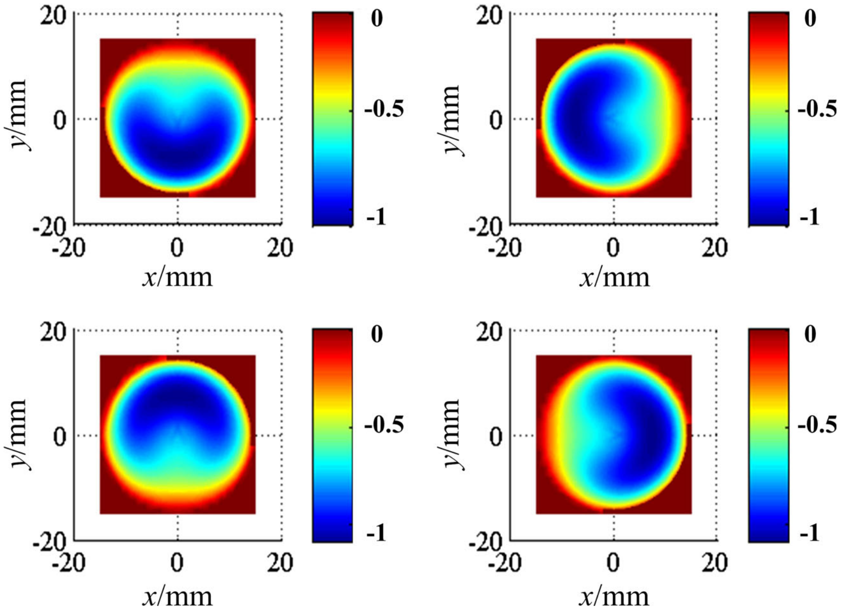

Fig. 14 Normalized TIF of tilted polishing in four directions

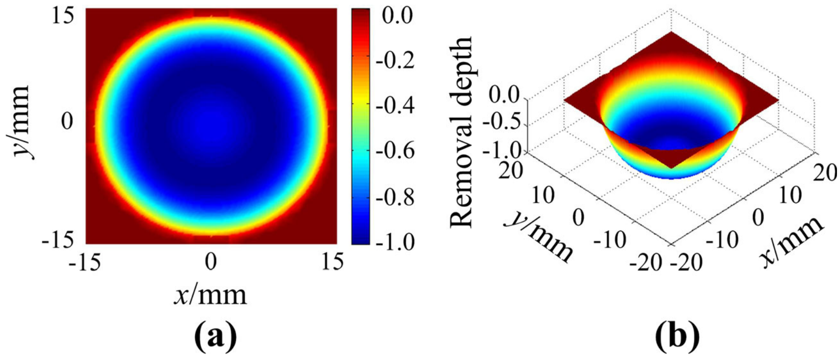

Fig. 15 Normalized 4-discrete precession polishing TIF. **a** Top view, **b** isometric view

polishing, which includes four times tilted polishing in four different directions.

According to the movement model in Fig. 10, the velocity of point $Q(x, y)$ in the contact area of tilted polishing can be expressed as

$$v_Q = \sqrt{\omega_1{}^2[(R-l)\sin\alpha - y\cos\alpha]^2 + \omega_1{}^2x^2\cos^2\alpha} \quad (5)$$

Then, the velocity distribution in the contact area of four directions can be simulated in MATLAB as shown in Fig. 12. The calculated velocity distribution result is actually a two-dimensional matrix mapping to the x–y plain. From Fig. 12, we can see that the contact zone further from the rotation axis has a larger velocity value.

4.2 TIF simulation

The contact pressure with tool offset 1.6 mm has been extracted from the simulation results shown in Fig. 8b, and processed

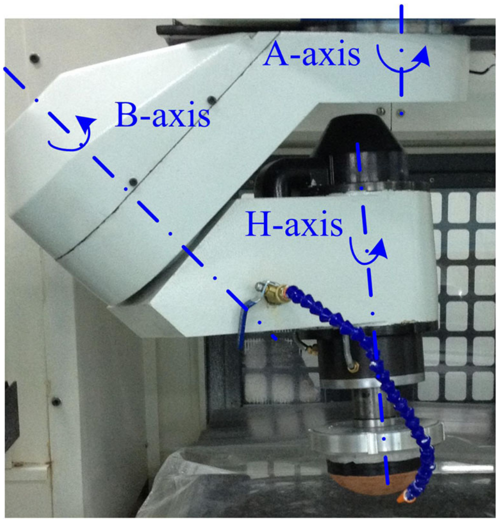

Fig. 16 Experimental device

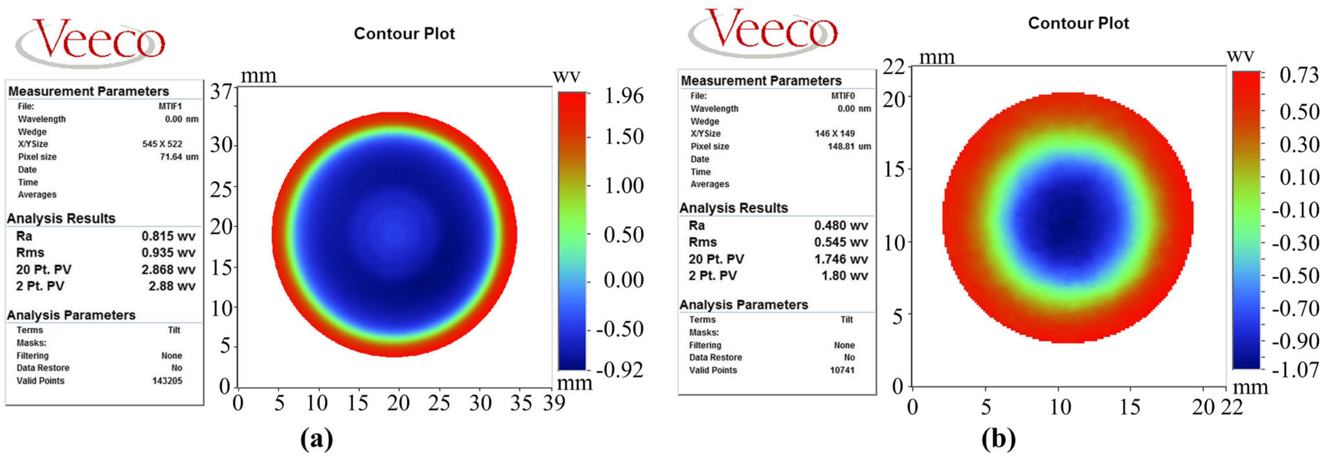

Measurement Parameters	
File:	MTIF1
Wavelength	0.00 nm
Wedge	
X/YSize	545 X 522
Pixel size	71.64 um
Date	
Time	
Averages	

Analysis Results	
Ra	0.815 wv
Rms	0.935 wv
20 Pt. PV	2.868 wv
2 Pt. PV	2.88 wv

Analysis Parameters	
Terms	Tilt
Masks:	
Filtering	None
Data Restore	No
Valid Points	143205

Measurement Parameters	
File:	MTIF0
Wavelength	0.00 nm
Wedge	
X/YSize	146 X 149
Pixel size	148.81 um
Date	
Time	
Averages	

Analysis Results	
Ra	0.480 wv
Rms	0.545 wv
20 Pt. PV	1.746 wv
2 Pt. PV	1.80 wv

Analysis Parameters	
Terms	Tilt
Masks:	
Filtering	None
Data Restore	No
Valid Points	10741

Fig. 17 Measured polishing spots. **a** TIF 1: tool offset=1.6 mm, **b** TIF 2: tool offset=0.5 mm

Fig. 18 Comparison of the sectional profiles between simulated TIF and measured TIF. **a** TIF 1, **b** TIF 2

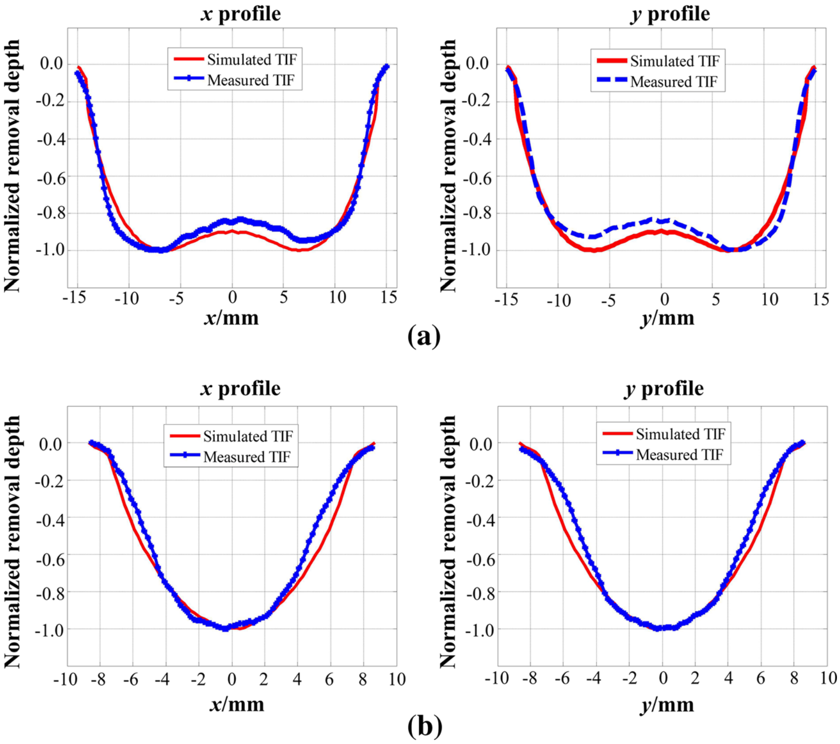

Fig. 19 Residual error between the simulation TIFs and measured TIFs. **a** TIF 1, **b** TIF 2

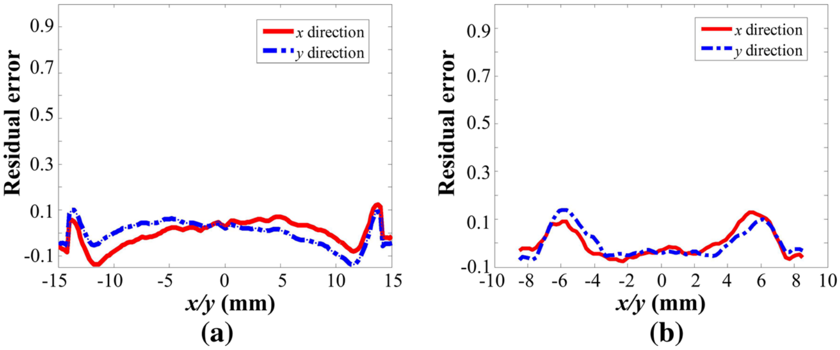

to be a two-dimensional matrix which has the same elements with the velocity distribution matrix in MATLAB. Figure 13 shows the contact pressure distribution in four directions corresponding to Fig. 12.

Combining the contact pressure matrixes and velocity distribution matrixes, normalized TIF can be obtained as shown in Fig. 14. Shapes of these TIFs are similar to their contact pressure distribution. Then, the 4-discrete precession polishing TIF can be simulated through the superposition of these four tilted polishing TIFs, which has been presented in Fig. 15. Through the superposition, the velocity and contact pressure can be averaged in the contact area, leading to the shape of 4-discrete precession polishing TIF being a rotational symmetric M shape.

5 Experimental verifications

To verify the accuracy of the TIF model, experiments generating two polishing spots under different tool offsets were conducted. Figure 16 shows the experimental device. *A*-axis and *H*-axis are corresponding to Fig. 10. *B*-axis controls the precession angle α. Spots are generated on BK7 parts using ~1.5 wt% CeO_2 polishing slurry. Tool offsets of these two spots are 0.5 and 1.6 mm, respectively. Other experimental conditions are the same as the simulation conditions as shown in Table 2. The dwell time of each spot is 8 s. Figure 17 shows the measurement results of these two spots. The shape of the spot when tool offset is 1.6 mm is M shaped, which is the same as the simulation results. And the shape of the spot when tool offset is 0.5 mm is Gaussian like. To compare the simulation results and the experimental results quantitatively, both the *x*/*y* sectional profiles of the simulated and experimental results have been extracted out and normalized as shown in Fig. 18.

As demonstrated in Fig. 18, both of these two simulated TIFs are in good agreement with the measured TIFs. Their residual errors have been presented in Fig. 19. The relative deviation between the simulated and experimental results of TIF 1 is 5.93 % in the *x* direction and 5.69 % in the *y* direction, and 5.84 % in the *x* direction and 5.89 % in the *y* direction for TIF 2 in terms of root mean square of the residual error. The deviation may be induced by the effect of the polishing pad and the polishing slurry.

6 Conclusions

For BP, M-shaped TIF is as important as Gaussian-like TIF. A TIF model is presented based on the optimized finite element simulation model for contact pressure. The pressure distribution used in this model is generated directly based on the simulation result rather than fitting the simulated data using an equation. Hence, it can not only be used to model the M-shaped TIF used in high-efficiency polishing stage but also can be used to model the Gaussian-like TIF. The verification experiments show that the simulated TIFs based on this model are in good agreement with the actual measured TIF, which proves the effectiveness of this model.

Acknowledgments This work was financially supported by major national science and technology projects (Grant No. 2013ZX04006011-206) and the Science Technology Project of Xiamen City (Grant No. 3502Z20133036). We also appreciate the invaluable expert comments and advice on the manuscript from all anonymous reviewers.

References

1. Bingham RG, Walker DD, Kim DH, Brooks D, Freeman R, Riley D (2000) Novel automated process for aspheric surfaces. Proc SPIE 4093:281–289
2. Walker DD, Brooks D, King A, Freeman R, Morton R, McCavana G, Kim SW (2003) The ‘Precessions’ tooling for polishing and figuring flat, spherical and aspheric surfaces. Opt Express 11(8): 958–964
3. Walker DD, Freeman R, Morton R, McCavana G, Beaucamp A (2006) Use of the ‘Precessions’ TM process for prepolishing and correcting 2D & 21/2D form. Opt Express 14(24):11787–11795
4. Walker DD, Yu GY, Li HY, Messelink W, Evans R, Beaucamp A (2012) Edges in CNC polishing: from mirror-segments towards semiconductors, paper 1: edges on processing the global surface. Opt Express 20(18):19787–19798
5. Wang CJ, Yang W, Ye SW, Wang ZZ, Yang P, Peng YF, Guo YB, Xu Q (2014) Restraint of tool path ripple based on the optimization of tool step size for sub-aperture deterministic polishing. Int J Adv Manuf Technol 75(9–12):1431–1438
6. Zeng S, Blunt L (2014) An experimental study on the correlation of polishing force and material removal for bonnet polishing of cobalt chrome alloy. Int J Adv Manuf Technol 73(1–4):185–193
7. Jing HW, King C, Walker DD (2010) Measurement of influence function using swing arm profilometer and laser tracker. Opt Express 18(5):5271–5281
8. Yi HS, Yang HS, Lee YW, Kim SW (2011) Kernel TIF method for effective material removal control in rotating pitch tool-based optical figuring. Int J Adv Manuf Technol 55(1–4):75–81
9. Liao WL, Dai YF, Xie XH, Zhou L (2014) Mathematical modeling and application of removal functions during deterministic ion beam figuring of optical surfaces. Part 1: mathematical modeling. Appl Opt 53(19):4266–4274
10. DeGroote JE, Marino AE, Wilson JP, Bishop AL, Lambropoulos JC, Jacobs SD (2007) Removal rate model for magnetorheological finishing of glass. Appl Opt 46(32):7927–7941
11. Kordonski W, Gorodkin S (2011) Material removal in magnetorhelogical finishing of optics. Appl Opt 50(14):1984–1994
12. Li ZZ, Li SY, Dai YF, Peng XQ (2010) Optimization and application of influence function in abrasive jet polishing. Appl Opt 49(15):2947–2953
13. Beaucamp A, Namba Y, Freeman R (2012) Dynamic multiphase modeling and optimization of fluid jet polishing process. Ann CIRP 61(1):315–318
14. Kim DW, Burge JH (2009) Rigid conformal polishing tool using non-linear visco-elastic effect. Opt Express 18(3):2242–2257

15. Kim DW, Kin SW (2005) Static tool influence function for fabrication simulation of hexagonal mirror segments for extremely large telescopes. Opt Express 13(3):910–917
16. Li HY, Walker DD, Yu GY, Zhang W (2013) Modeling and validation of polishing tool influence functions for manufacturing segments for an extremely large telescope. Appl Opt 52(23):5781–5787
17. Wang CJ, Wang ZZ, Yang X, Sun ZJ, Peng YF, Guo YB, Xu Q (2014) Modeling of the static tool influence function of bonnet polishing based on FEA. Int J Adv Manuf Technol 74(1–4):341–349
18. Wang CJ, Yang W, Wang ZZ, Yang X, Sun ZJ, Zhong B, Pan R, Yang P, Guo YB, Xu Q (2014) Highly efficient deterministic polishing using a semirigid bonnet. Opt Eng 53(9):095102
19. Kim C, Lee SB, Lee J, Cho S, Park H, Yeom S, Park SH (2012) A comparison among neo-Hookean model, Mooney-Rivlin model, and Ogden model for chloroprene rubber. Int J Precis Eng Manuf 13(5):759–764
20. Kawamura T, Urayama K, Kohjiya S (2003) Multiaxial deformations of end-linked poly(dimethylsiloxane) networks 5. Revisit to Mooney-Rivlin approach to strain energy density function. J Soc Rheol 31(4):213–217
21. Zeng S, Blunt L (2014) Experimental investigation and analytical modeling of the effects of process parameters on material removal rate for bonnet polishing of cobalt chrome alloy. Prescis Eng 38(2):348–355
22. Pan R, Wang ZZ, Jiang T, Wang ZS, Guo YB (2015) A novel method for aspheric polishing based on abrasive trajectories analysis on contact region. Proc IMechE B J Eng Manuf 229(2):275–285
23. Pan R, Zhang YJ, Ding JB, Wang ZZ, Guo YB (2015) Research on optimization of conformal polishing using continuous precession. Int J Adv Manuf Technol 78(1–4):63–71